Two-Segment High-Performance PV Grid-Connected Inverter

Ancheng Liu, *Student Member, IEEE*, Yipei Wang, Taeho Kwon, and Sung-Jun Park, *Member, IEEE*

***Abstract*—In PV grid-connected applications, a grid-connected converter is usually used to connect with the grid to realize dc/ac conversion and power flow control. How to improve the quality of grid-connected current of power equipment so that the harmonic content injected into the grid is as little as possible has become a hot research topic in the field of PV grid-connected applications. By analyzing the causes of grid-connected harmonic currents during the grid-connection process, a two-segment high-performance grid-connected inverter topology is proposed. This structure makes the main inverter basically equal to the grid voltage through the simplest closed-loop control. Since the voltage sensitivity of the auxiliary inverter is low, utilizing the auxiliary inverter for the compensation of grid-connected voltage and grid-connected control of power flow will lead to an improvement in the quality of grid-connected current. A 3.3 kW grid-connected inverter system prototype is fabricated and tested, and the experimental results verify the stability and effectiveness of the theoretical analysis and the proposed control scheme.**

***Index Terms*—Harmonic suppression, photovoltaic grid-connected inverter, total harmonic distortion (THD), voltage sensitivity.**

I. Introduction

With the widespread adoption of photovoltaic power generation technology, PV grid-connected inverters, serving as the interface for ac/dc conversion, are being increasingly integrated into the load side of power grids and have become a significant factor affecting the quality of electrical energy in the grid [1], [2]. The most commonly used and simple grid-connected inverter is shown in Fig. 1. Despite the numerous advantages of grid-connected converters, they are still nonlinear power electronic devices, and factors such as dc side ripple and switch dead time inevitably introduce a significant amount of harmonic current into the common grid [3], [4], [5]. Generally,

Received 3 January 2024; revised 23 April 2024, 28 June 2024, and 7 September 2024; accepted 8 October 2024. Date of publication 15 October 2024; date of current version 18 December 2024. This work was supported in part by the Gwangju Jeonnam Local Energy Cluster Human Resources Development of the Korea Insitute of Energy Technology Evaluation and in part by the Planning (KETEP) grant funded by the Korea government Ministry of Trade, Industry and Energy under Grant 20214000000560. Recommended for publication by Associate Editor D. Vinnikov. *(Corresponding author: Sung-Jun Park.)*

Ancheng Liu, Yipei Wang, and Sung-Jun Park are with the Department of Electrical Engineering, Chonnam National University, Gwangju 61186, South Korea (e-mail: anchengliu96@gmail.com; wangyipeijn@gmail.com; sjpark1@jnu.ac.kr).

Taeho Kwon is with Gyeonglim Company Ltd., Gyeongnam 52249, South Korea (e-mail: xogh2507@naver.com).

Color versions of one or more figures in this article are available at https://doi.org/10.1109/TPEL.2024.3480994.

Digital Object Identifier 10.1109/TPEL.2024.3480994

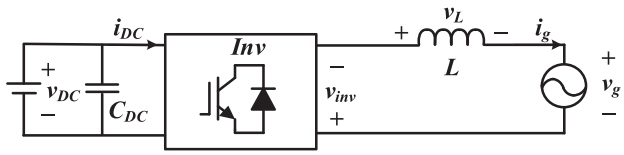

Fig. 1. *L* filter grid-connected structure.

the harmonic distortion of the grid current caused by the inherent nonlinear characteristics of grid-connected inverters is an important metric for assessing the quality of grid-connected current [6]. Harmonic currents can lead to a series of hazards. For instance, they can cause harmonic losses, reducing the efficiency of electrical power transmission in the grid; degrade the performance of electrical equipment and interfere with nearby communication systems; and trigger the malfunction of electric protection equipment, leading to power outages [7], [8], [9].

The ac side power has a pulsating quadratic component in addition to the stabilized direct current. According to the principle of conservation of energy, the dc side must provide this two-fold power for it, and therefore a two-fold voltage fluctuation also occurs on the dc side capacitor voltage [10], [11]. The use of the virtual impedance control method is proposed in both [12] and [13] to reduce the dc second harmonic current. Experiments verified that the method can effectively reduce the second harmonic content, but the complexity of the control system is greatly increased. This complexity may lead to system stability problems. Zhou et al. [14] proposed a method to suppress second harmonic currents using a high-gain dc–dc converter with accurate small-signal modeling and impedance editing, which can effectively improve stability and efficiency. However, the experimental power conducted is low and its generalization needs to be further determined. A new inverter second harmonic injection strategy for PV dc booster systems is proposed in [15] to enable fast recovery to maximum power point tracking control without additional communication after grid disturbances, thus improving power generation efficiency. A new electrolytic capacitor's second harmonic current compensator (SHCC) is introduced in [16], which uses hybrid single-cycle control to regulate the SHCC. However, the losses and costs are increased because of the additional equipment. [17] introduced a method using a dc transformer *LLC* resonant converter to suppress second harmonic currents in the front-end dc–dc converter of two-stage inverters, employing control strategies such as notch filters and virtual impedances, which requires precisely designed control parameters as incorrect implementation may

severely compromise system stability. [18] employs a high-gain front-end dc–dc converter with inductor current feedback and an active damping scheme to enhance stability and efficiency.

In a full-bridge converter composed of fully controlled devices, a dead time must be added to the switching signals of the upper and lower switches of the same bridge arm to prevent the bridge arm from damaging the switching devices with a straight-through fault. The existence of this dead time makes the actual output voltage of the inverter deviate from the ideal voltage [19], [20], [21] analyzes disturbances caused by inverter deadtime in feedback quantizer modulation (FBQM) and proposes specific deadtime compensation techniques within the FBQM framework, albeit with certain limitations. Tang et al. [22] propose a real-time compensation method for inverter nonlinearity by estimating the deadtime effect based on the variance in voltage error across continuous and discontinuous PWM schemes. A simple and improved active voltage clamped highly efficient and reliable inverter concept modulation scheme is proposed in [23] to improve the power quality by compensating the dead zone and minimizing the pulse width distortion. However, the proposed scheme may limit its applicability to other inverter types. Zheng et al. [24] present a fully digital soft-switching control for inverters in critical conduction mode, utilizing variable OFF-time and deadtime to optimize digital control frequency, balancing high performance with computational efficiency.

The most commonly used grid-connected structure is still the *LCL* filter grid-connected structure, and there are many control methods regarding the *LCL* structure. Bahrami-Fard et al. [9] present a novel feedback strategy using capacitor voltage to enhance the current quality of *LCL*-type grid-connected inverters. Ma et al. [25] proposes an active disturbance rejection control (ADRC) strategy for *LCL*-type grid-connected inverters, enhancing stability and robustness by optimizing resonance damping and adapting to filter parameter perturbations. Tran et al. [26] introduce a robust, optimized ADRC strategy for an *LCL*-filtered grid-connected inverter, utilizing a resonant extended state observer and predictive control to enhance sinusoidal reference tracking and disturbance rejection in varied grid conditions. Active power filters are widely used in grid-connected systems to improve power quality. Karbasforooshan and Monfared [27] introduce an adaptive self-tuned current controller for a single-phase shunt hybrid active power filter with *LCL*-filtered *LC*-tuning, which dynamically adjusts to parameter changes. Bosch et al. [28] presents a predictive current control scheme for a three-phase four-wire *LCL*-filter-based active power filter, designed to enhance the management of harmonic currents without increasing computational demands.

To improve photovoltaic grid-connected current quality, diverse filter topologies for PV inverters have been developed [29]. A passivity-based parameter design method for *LLCL*-filtered grid-connected inverters was proposed in [30], with experimental validation confirming stable operation across various grid impedances, though the multiple resonant circuits could lead to increased costs and space requirements. An integrated active EMI filter was introduced in [31] for V2G systems, offering enhanced harmonic suppression and EMI noise reduction without external passive components. A control strategy that reduces system order from third to first for grid-connected inverters with *LCCL* filters, incorporating differential feedforward and grid voltage feedforward mechanisms, was presented in [32]. The *LTCL* filter proposed in [33] provides increased harmonic attenuation without adding control complexity, yet the complexity of the filter itself may increase the system's sensitivity and decrease its stability.

In recent years, in addition to the traditional PV grid-connected inverters, many new PV grid-connected inverters have emerged [38], [39], [40]. Pourfarrokh et al. [38] introduce an asymmetrical multilevel inverter for PV systems, utilizing a unidirectional isolated dc–dc converter to increase PV voltage, prevent reverse power flow, and enhance efficiency and stability. Rahimi et al. [40] present a filter-clamped three-phase grid-connected transformerless PV inverter that reduces leakage current, improves grid current THD, and enhances overall efficiency without adding extra components or modifying control techniques.

Most harmonic suppression methods for the grid-connected current focus on harmonics produced by the inverters, with less consideration for background harmonic influences. Two common approaches are used for suppression [34]: one involves increasing the current loop gain at harmonic frequencies with multiresonant or multisynchronous regulators, which can lead to instability if harmonics are near the current loop crossover frequency [35]; the other employs a grid voltage feedforward scheme that effectively suppresses low-frequency harmonics but may amplify higher frequencies [36]. Measuring grid voltage directly can be challenging, especially in weak grids or when inverters are connected through transformers, often leading to the use of the point of common coupling filter capacitor voltage instead [37]. This article focuses on analysis from the grid side and proposes a two-segment grid-connected inverter structure, highlighting several key contributions.

1) A photovoltaic grid-connected inverter system has been designed, employing the proposed two-segment grid-connected inverter structure. The main inverter generates a voltage similar to the grid voltage, while the auxiliary inverter carries out grid connection control. This method effectively reduces the voltage sensitivity of the topology, enabling high-quality grid connection even with simple PI control, thereby significantly reducing the harmonic content of the grid current.
2) Introducing an auxiliary inverter in a two-segment system requires additional power electronic components, thereby increasing hardware costs. However, the sensors and control methods needed for the main inverter are very simple, allowing for mass production and cost advantages. Therefore, the added costs mainly come from the auxiliary inverter used for grid connection control. Although the system structure is relatively complex, its control method is much simpler than the commonly used *LCL* filter grid connection approach, which should reduce failure rates and maintenance costs. Although the initial cost of the two-segment system is higher, it significantly improves system efficiency while reducing installation and maintenance costs, demonstrating long-term economic benefits.

3) To verify the effectiveness of the proposed topology scheme, a 3.3 kW two-segment PV grid-connected inverter prototype is fabricated and tested. The experimental results show that the scheme proposed in this article enhances the reliability and flexibility of the system while improving the grid-connection effect.

II. Proposed Two-Segment Grid-Connected Inverter Structure

A. Influencing Factors

In a single-phase grid-connected system, voltage and current can be expressed as

$$\dot{i_g} = \frac{1}{L}(v_{\text{inv}} - v_g) \tag{1}$$

where v_{inv} is the output voltage of the PV grid-connected inverter, v_g is the grid voltage, and L is the inductance of the filter

$$i_g = \frac{1}{L}\int\left[\left(v_{\text{inv}1} + \sum_{h=2}^{n} v_{\text{inv}h}\right) - \left(v_{g1} + \sum_{h=2}^{n} v_{gh}\right)\right]. \tag{2}$$

The above expression yields

$$i_g = \underbrace{\frac{1}{L}\int (v_{\text{inv}1} - v_{g1})}_{i_{g1}} + \underbrace{\frac{1}{L}\int\left(\sum_{h=2}^{n} v_{\text{inv}h} - \sum_{h=2}^{n} v_{gh}\right)}_{\sum_{h=2}^{n} i_{gh}} \tag{3}$$

where i_{g1} denotes a fundamental component of the injected grid, which is obtained from a fundamental component $v_{\text{inv}1}$ of the inverter output voltage and a fundamental component v_{g1} of the grid voltage. $\sum_{h=2}^{n} i_{gh}$ denotes a harmonic component of the injected grid, which is obtained from a harmonic component $\sum_{h=2}^{n} v_{\text{inv}h}$ of the inverter output voltage and a harmonic component $\sum_{h=2}^{n} v_{gh}$ of the grid voltage.

As can be seen from (3), the harmonics in the grid current are caused by both the harmonic voltages from the grid-connected inverter and the grid itself. Therefore, if appropriate control methods or modulation techniques are applied to the grid-connected inverter such that the harmonic content of its output voltage equals that of the grid voltage ($\sum_{h=2}^{n} v_{\text{inv}h} = \sum_{h=2}^{n} v_{gh}$), it is possible to eliminate harmonic currents caused by grid voltage harmonics. Of course, this is an ideal scenario. However, it is typically challenging to precisely control the output voltage harmonics of an inverter, which in turn affects the quality of the grid current.

Since the grid voltage distortion is usually uncontrolled and mainly caused by nonlinear loads connected to the grid, we can only qualitatively analyze the inverter output voltage harmonics. To analyze the harmonics generated by the inverter output voltage, the grid voltage is regarded as a standard sine wave without harmonics. The following is a detailed analysis of the dead zone effect and the harmonic current generation mechanism caused by the second ripple voltage on the dc side.

The unipolar frequency doubling modulation case u_{dead} can be expressed in one switching cycle as

$$u_{\text{dead}}(t) = \begin{cases} -\frac{2t_d}{T_{sw}} v_{\text{dc}} & i_g > 0 \\ \frac{2t_d}{T_{sw}} v_{\text{dc}} & i_g < 0 \end{cases} \tag{4}$$

where u_{dead} is the error voltage due to the deadtime effect, T_{sw} is the switching period, and t_d is the deadtime. A simplification of (4) is obtained as

$$u_{\text{dead}}(t) = -\frac{2t_d}{T_{\text{sw}}} v_{\text{dc}} \text{sgn}(i_g). \tag{5}$$

To facilitate the quantitative analysis of the impact of the dead zone effect, it is assumed that the

$$i_g(t) = A\sin(\omega t + \theta) \tag{6}$$

where A, ω, and θ are the amplitude, angular frequency, and phase of the current $i_g(t)$, respectively. Therefore, $\text{sgn}(i_g)$ is a periodic function of period $2\ \pi/\omega$ concerning time t, and its Fourier series expansion yields

$$\begin{cases} \text{sgn}(t) = \text{sgn}\left[A\sin(\omega t + \theta)\right] \\ a_0 = \frac{2}{2\pi}\int_{-\pi}^{\pi} \text{sgn}(i_g) d(\omega t + \theta) = 0 \\ a_n = \frac{2}{2\pi}\int_{-\pi}^{\pi} \text{sgn}(i_g)\cos n(\omega t + \theta) d(\omega t + \theta) = 0 \\ b_n = \frac{2}{2\pi}\int_{-\pi}^{\pi} \text{sgn}(i_g)\sin n(\omega t + \theta) d(\omega t + \theta) \\ = \begin{cases} \frac{4}{n\pi}, n = 1, 3, 5 \ldots \\ 0, n = 2, 4, 6 \ldots \end{cases} \end{cases}. \tag{7}$$

From (7) one can further obtain as

$$\text{sgn}(t) = \sum_{n=1,3,5\ldots} \frac{4}{n\pi}\sin n(\omega t + \theta). \tag{8}$$

Therefore, expanding the u_{dead} using the Fourier series can be obtained as

$$u_{\text{dead}}(t) = -\frac{8t_d v_{\text{dc}}}{\pi T_{\text{sw}}} \sum_{n=1,3,5\ldots} \frac{1}{n}\sin n(\omega t + \theta). \tag{9}$$

From (9), it can be seen that the error voltage u_{dead} consists of the fundamental wave and a series of odd harmonic components, leading to the corresponding frequency of the grid-side harmonic currents. Its amplitude is proportional to v_{dc} and t_d, and inversely proportional to T_{sw} and the number of harmonics n.

Assume that the fundamental grid voltage v_{g1} and the fundamental grid current i_{g1} are shown as

$$\begin{cases} v_{g1} = \sqrt{2} V_{g1}\cos(\omega t + \varphi) \\ i_{g1} = \sqrt{2} I_{g1}\cos(\omega t) \end{cases} \tag{10}$$

where V_{g1} is the magnitude of v_{g1}, I_{g1} is the magnitude of i_{g1}, φ is the phase difference between v_{g1} and i_{g1}, and ω is the angular frequency of v_{g1}. Then the instantaneous power P_{inv} at the ac side of the grid-connected converter is

$$P_{\text{inv}} = v_{\text{inv}1} i_{g1} = V_{\text{inv}1} I_{g1}\left[1 - \cos(2\omega t)\right]. \tag{11}$$

The instantaneous power on the dc side can be expressed as follows:

$$P_{\text{dc}} = V_{\text{dc}} I_{\text{dc}} + C_{\text{dc}} V_{\text{dc}} \frac{d\tilde{v}_{\text{dc}}}{dt} \tag{12}$$

TABLE I
PARAMETERS OF THE FILTER MODULE

	Parameters	Symbol	value
LC inverter	Dc-link voltage	v_{dc}	400 V
	Grid-connected inductance	L_f	1.5 mH
	Grid-connected capacitance	C_f	6.6 μF
	Sampling frequency	f_s	16.2 kHz
	Switching frequency	f_{sw}	16.2 kHz
Main inverter	Dc-link voltage	v_{dc_m}	400 V
	Grid-connected inductance	L_m	1.5 mH
	Grid-connected capacitance	C_a	6.6 μF
	Sampling frequency	f_{s_m}	16.2 kHz
	Switching frequency	f_{sw_m}	16.2 kHz
Auxiliary inverter	Dc-link voltage	v_{dc_a}	48 V
	Grid-connected inductance	$L_{a1}+L_{a2}$	66 μH
	Grid-connected capacitance	C_m	10 μF
	Sampling frequency	f_{s_a}	10 kHz
	Switching frequency	f_{sw_a}	20 kHz

where $V_{\rm dc}$ is the average value of dc side voltage, $I_{\rm dc}$ is the average value of dc side current, and $\tilde{v}_{\rm dc}$ is the dc side pulsating voltage.

From (11) and (12), it can be seen that the instantaneous power on both ac and dc sides consists of constant power and pulsating power. Assume that the grid-connected converter operates in an ideal state with no energy loss. Then, according to the conservation of instantaneous power on the ac side and dc side, i.e., the corresponding constant power and pulsating power are equal, (13) can be obtained as

$$\begin{cases} V_{\rm dc} I_{\rm dc} = V_{\rm inv1} I_{g1} \\ C_{\rm dc} V_{\rm dc} \frac{d\tilde{v}_{\rm dc}}{dt} = V_{\rm inv1} I_{g1} \cos(2\omega t) \end{cases}. \tag{13}$$

From (13), the dc side pulsating voltage is

$$\tilde{v}_{\rm dc} = \frac{V_{\rm inv1} I_{g1}}{2\omega C_{\rm dc} V_{\rm dc}} \sin(2\omega t). \tag{14}$$

From (14), the frequency of this pulsating voltage is twice the frequency of the fundamental wave. The $\tilde{v}_{\rm dc}$ amplitude is proportional to $V_{\rm inv1}$ and I_{g1} and inversely proportional to $C_{\rm dc}$ and $V_{\rm dc}$. The dc side voltage $v_{\rm dc}$ consists of the average voltage $V_{\rm dc}$ and the secondary ripple voltage $\tilde{v}_{\rm dc}$ superimposed as shown in

$$v_{\rm dc} = V_{\rm dc} + \tilde{v}_{\rm dc}. \tag{15}$$

According to (9) and (14) combined with the data in Table I it can be obtained that the auxiliary inverter is smaller than the main inverter both in terms of the second harmonic of the dc side and the error voltage $u_{\rm dead}$. Therefore, it can be obtained that the voltage harmonics generated by the auxiliary inverter are much smaller than the harmonic voltage generated by the main inverter.

B. Proposed Structure

In a single-phase grid-connected power generation system, when using a high-frequency PWM switching inverter, its high-frequency modulation will produce a large number of harmonic components near the switching frequency. A passive filter is commonly used to effectively suppress these harmonics. A common passive filter is shown in Fig. 2.

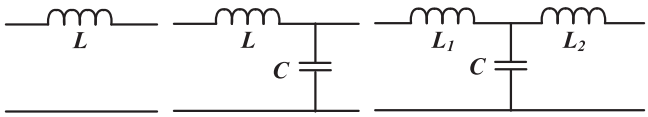

Fig. 2. Commonly used passive filter structures.

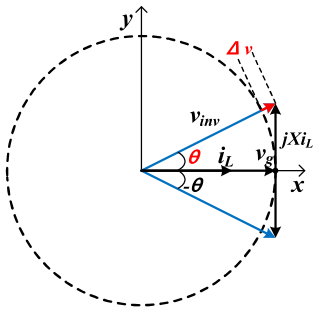

Fig. 3. *L*-type filtered grid-connected voltage and current vector diagram.

When an inverter operates in grid-connected mode, due to the clamping effect of the grid voltage, if an *LC*-type filter is used, the filtering capacitor acts like a load, and only the inductance functions as the filter, making the filtering effect equivalent to that of an *L*-type filter. Therefore, the most common and standard filters used in grid-connected inverters are the *L*-type first-order filter and the *LCL*-type third-order filter.

Taking an *L*-type grid-connected inverter as an example, the grid voltage and current are analyzed. The *L*-filter grid-connection structure is illustrated in Fig. 1. From the properties of inductance and the application of KVL, (16) and (17) can be derived as

$$v_L = j\omega i_L L \tag{16}$$

$$v_{\rm inv} = v_g + v_L. \tag{17}$$

Representing the aforementioned physical quantities in a vector diagram yields Fig. 3. With a fixed grid-connected current, the voltage across the inductor depends on the magnitude of the inductance.

To meet the grid connection requirements, the inverter voltage value $V_{\rm inv}$ needs to satisfy

$$V_g \le V_{\rm inv} \le \sqrt{\left(V_g{}^2 + V_L{}^2\right)}. \tag{18}$$

Generally speaking, the rated voltage of the inductor is about 5% of the grid voltage, and it is difficult for the actual *L*-type grid-connected inverter to achieve the grid-connected voltage with the exact same amplitude as the grid voltage, and there is generally an error of about 1%. When there is an error, the *L*-filtered grid-connected voltage and current vector diagram becomes Fig. 4.

It is assumed that a 3 mH inductor is used in an inverter with a rated power P_r of 3 kW. According to (18) and (19), the inverter voltage value $V_{\rm inv}$ is 220.5 V at rated operation and the voltage fluctuation Δv is very small at 0.5 V

$$V_{\rm inv} = \sqrt{\left(V_g{}^2 + V_L{}^2\right)}. \tag{19}$$

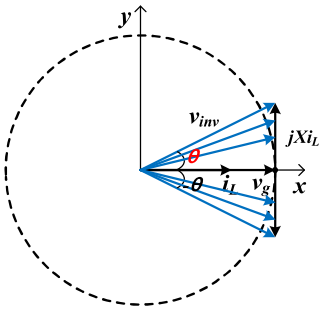

Fig. 4. *L*-type filtered grid-connected voltage and current vector diagram when an error exists.

The absolute value of v_{inv} minus the absolute value of v_{ac} is less than or equal to 0.2% of v_{inv}. Therefore, the rate of change of the inverter modulation ratio ΔM is expressed as less than or equal to 0.2%. At this time, the voltage across the inductor must be regulated by the inverter output voltage v_{inv}. In other words, the 15 V must be controlled by the 0–0.5 V generated by the inverter

$$|v_{\text{inv}}| - |v_g| \leq 0.2\% \tag{20}$$

$$\Delta M \leq 0.2\%. \tag{21}$$

In other words, the 15 V must be controlled by the 0–0.5 V generated by the inverter. Therefore, the voltage sensitivity is

$$s_v = \frac{\Delta v}{\Delta M} = \frac{15}{0.2\%} = 6818. \tag{22}$$

This illustrates that due to grid-connected operation, the output power is highly sensitive to the magnitude of the grid-connected inverter's output voltage, leading to difficulties in precisely controlling the output grid voltage. To address this issue, an *LCL* filter grid-connection structure is commonly employed in engineering to reduce the harmonic content of the grid current. By adding an additional inductance on the grid current side, some of the harmonic content is diverted to the capacitor, resulting in better attenuation at high frequencies and effective suppression of harmonic components. However, at the resonance frequency, there is a resonance peak that necessitates the addition of closed-loop control for suppression, which requires precise control and high stability. Additionally, the system's voltage sensors require low-pass filters with high cutoff frequencies; however, under such conditions, they are easily affected by noise. Therefore, new topological structures are required to eliminate the effects of grid harmonic voltage components.

In response to the drawbacks of the grid connection mentioned above, Fig. 5 displays a proposed two-segment grid-connected inverter topology. This configuration consists of a main inverter Inv_{main} and an auxiliary inverter, Inv_{aux}, arranged in series. The Inv_{main} has a higher output power and is primarily responsible for generating a voltage that matches the grid voltage in magnitude and phase. The Inv_{aux}, with its lower output power, controls the voltage applied to the reactor by detecting and responding to the voltage difference between the grid voltage and the voltage produced by Inv_{main}.

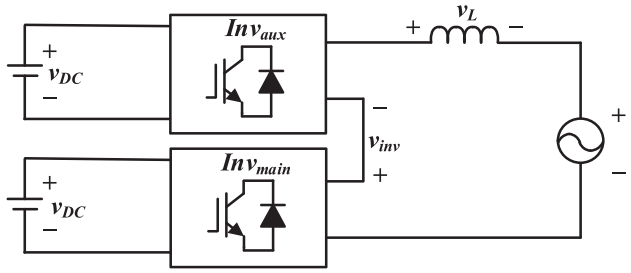

Fig. 5. Commonly used passive filter structures.

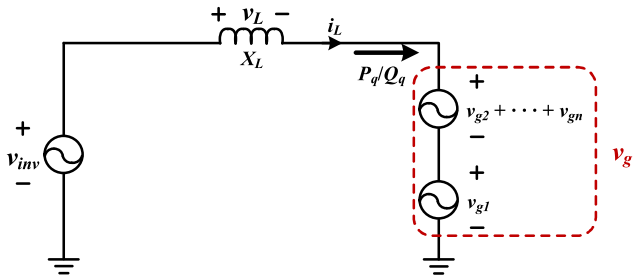

Fig. 6. Equivalent circuit diagram of *L*-type grid-connected inverter.

The main inverter only needs to generate a voltage that is close to or similar to the grid voltage. Once the program is set, it does not require further control. At this time, the voltage across the inductor can be adjusted by the output voltage v_a of the auxiliary inverter. In other words, the 15 V must be controlled by the auxiliary inverter with a modulation ratio ranging from 0 to 1. Therefore, the voltage sensitivity is

$$s_v' = \frac{\Delta v}{\Delta M'} = \frac{15}{1} = 15. \tag{23}$$

III. Structural and Control Analysis

A. Structural Analysis

During the grid-connection process, Fig. 1 can be equated to the circuit model shown in Fig. 6 if the presence of background harmonics is considered.

According to Fig. 6, due to the presence of grid voltage harmonics, a difference voltage between the grid voltage and the inverter output voltage is generated on the inductor as shown in

$$v_L = (v_{\text{inv}} - v_{g1}) - (v_{g2} + \cdots + v_{gn}). \tag{24}$$

This differential voltage leads to the inclusion of harmonic components in the current flowing toward the power grid, which in turn distorts the output current, resulting in an increase in the THD of the output current. In practical applications, it is essential to ensure that the THD content of the grid current remains below 5%. If the grid-connected power quality is not high, it will affect the power quality of the grid. This leads to an increase in the THD of the grid current, particularly for single-phase grid-connected systems. The two-segment grid-connected inverter proposed in Fig. 5 is equated to the circuit model shown in Fig. 7.

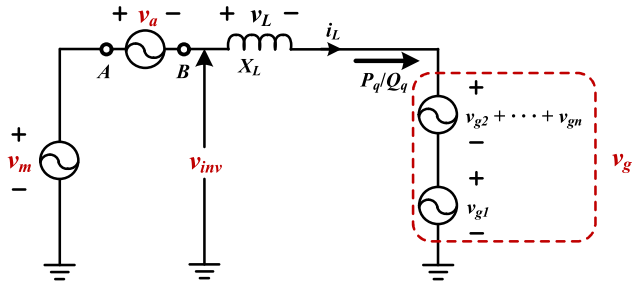

Fig. 7. Equivalent circuit diagram of the proposed two-segment grid-connected inverter.

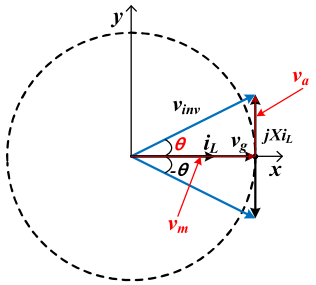

Fig. 8. Ideal state vector diagram.

In an ideal state, $\mathrm{Inv}_{\mathrm{main}}$ can bear all the harmonic voltages of the grid, as shown in

$$v_m = (v_L + v_a + v_{g1}) + (v_{g2} + \cdots + v_{gn}). \tag{25}$$

Upon conducting a qualitative analysis, if the harmonic voltage contained in v_m is equal to $(v_{g2}+\cdots+v_{gn})$, then in (26), v_L will only have the fundamental component and will not contain harmonic components. Consequently, the grid-connected current will also be free of harmonic content

$$v_L = v_{\mathrm{inv}} - v_g. \tag{26}$$

In reality, due to various errors and interferences, $\mathrm{Inv}_{\mathrm{main}}$ cannot accurately bear all the harmonic voltages of the grid. Suppose that the harmonic voltages contained in v'_m are equal to $(v'_{g2} + \cdots + v'_{gn})$, so that (27) can be obtained as

$$v'_m = (v'_L + v_a + v_{g1}) + (v_{g2} + \cdots + v_{gn}). \tag{27}$$

Therefore the harmonic content of v'_L in (28) is $(v_{g2} + \cdots + v_{gn}) - (v'_{g2} + \cdots + v'_{gn})$

$$v'_L = v'_m - v_a - v_g. \tag{28}$$

By comparing (26) and (28), it is evident that the harmonic content of v'_L is less than that of v_L. Therefore, it can be seen that the grid-connected current quality of the proposed two-segment grid-connected inverter is higher than that of the *L*-type grid-connected inverter.

The physical quantities in Fig. 5 are represented in a vector diagram, resulting in Fig. 8. Ideally, the grid voltage v_g is identical to the output voltage of the main inverter $\mathrm{Inv}_{\mathrm{main}}$, and the auxiliary inverter $\mathrm{Inv}_{\mathrm{aux}}$ only needs to control the voltage applied to the inductor. However, in reality, due to calculation errors or phase delays arising from voltage sensor and digital signal processor (DSP) sampling processes, a discrepancy occurs between the grid voltage and the output voltage of the main inverter. $\mathrm{Inv}_{\mathrm{aux}}$ must also compensate for this difference, as shown in Fig. 9.

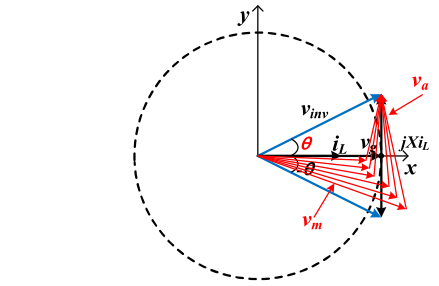

Fig. 9. Actual state vector diagram.

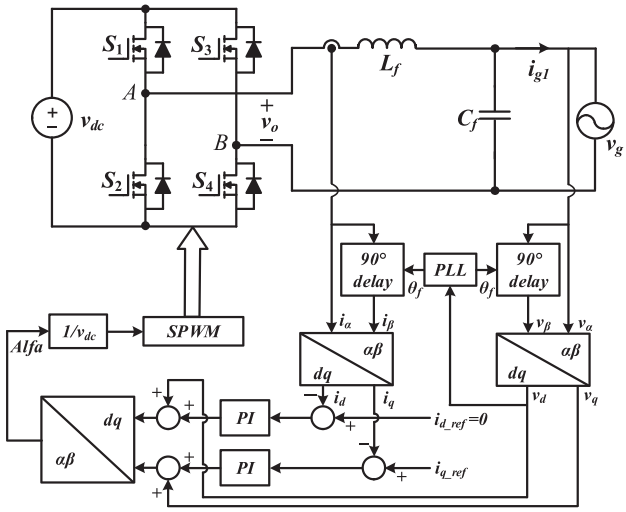

Fig. 10. Block diagram of conventional single-phase grid-connected inverter control.

The output voltage of the main inverter must be identical to the grid voltage, but there is typically a minor difference in amplitude and phase compared to the grid voltage. When the difference between the v_m and the grid voltage is as shown in Fig. 8, the output voltage of the auxiliary inverter v_a can correct this discrepancy. This adjustment ensures that the vector direction of the current i_L is equal to that of the grid voltage. At the same time, the orthogonal component *jxiL* can be controlled to the desired magnitude, thereby controlling the grid-connected current.

B. Control Methods

Fig. 10 depicts the control block diagram of a traditional single-phase grid-connected inverter. The system processes the feedback signals of the inverter's output current, output voltage, and grid voltage in real time via a DSP. Utilizing a phase-locked loop (PLL) and PI control algorithms, appropriate control signals are generated. These signals are further translated into

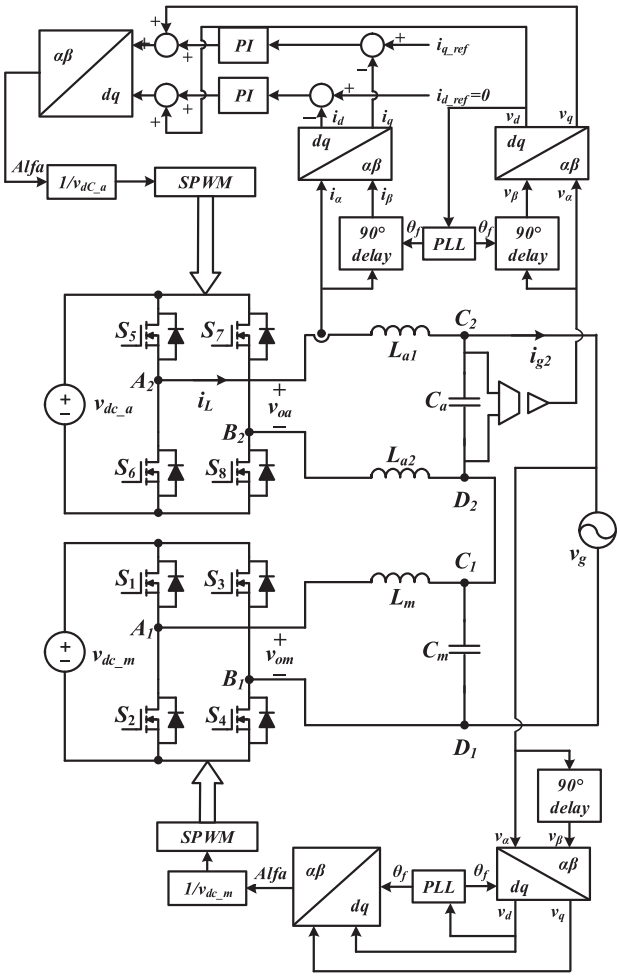

Fig. 11. Control block diagram of the proposed two-segment grid-connected inverter.

gate drive signals for the IGBT through a sinusoidal pulsewidth modulation (SPWM) modulator.

As shown in Fig. 11, the control of the proposed two-segment grid-connected inverter consists of two portions, namely, the control of the main inverter $\mathrm{Inv}_{\mathrm{main}}$ and the control of the auxiliary inverter $\mathrm{Inv}_{\mathrm{aux}}$. The control of $\mathrm{Inv}_{\mathrm{main}}$ adopts the straightforward closed-loop control, in which the amplitude and phase of the grid are obtained from the voltage transformer, and then the control signals of $S_1 \sim S_4$ are derived through PLL and modulation ratio. The control of $\mathrm{Inv}_{\mathrm{aux}}$ adopts the same control method as that of the traditional grid-connected inverter, and the defined reference currents i_{d_ref} and i_{q_ref} are passed through the PI controller with voltage feedforward to obtain the control signals of $S_5 \sim S_8$.

The closed-loop feedback control block diagram with voltage feedforward utilized in Fig. 10 has been simplified as shown in Fig. 12.

Fig. 12 depicts the structure of a classical grid-connected control system, which achieves the goal of precise control of the output current by employing a finely designed closed-loop feedback and feedforward compensation strategy. Where $i^*_L(s)$ denotes the current reference signal, $i_L(s)$ is the actual current

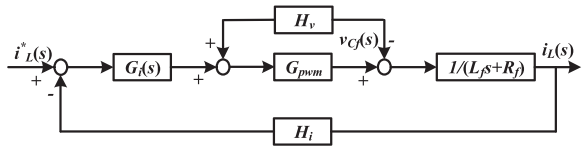

Fig. 12. Control block diagram of the conventional structure.

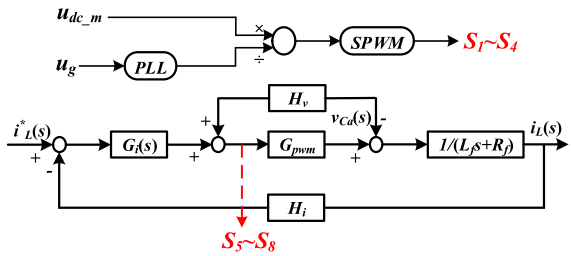

Fig. 13. Control block diagram of the proposed structure.

of the inductor, and $v_{Cf}(s)$ is the voltage across the capacitor. H_v and H_i are the sampling coefficients of the voltage and the current, and $G_i(s)$ is the current-loop controller with PI control. G_{pwm} is the gain of the PWM modulator, and R_f is the equivalent series resistance of L_f.

The actual current $i_L(s)$ is fed back through the sensor with transfer function Hi, and the difference with the current reference signal $i^*_L(s)$ is obtained as the input of PI control. The control signal from the PI controller is then compensated by voltage feedforward to obtain the final voltage control signal. The design of the feedforward compensation aims to further improve the system's tracking of the reference signal and suppress specific disturbances. The control block diagram employed in Fig. 11 has been simplified as shown in Fig. 13.

The diagram indicates that the control method for the auxiliary inverter $\mathrm{Inv}_{\mathrm{aux}}$, is identical to that of a conventional grid-connected inverter, with the only variation being in the value of the feedforward voltage. In a traditional grid-connected inverter, the feedforward voltage is derived from the grid voltage. However, for the auxiliary inverter $\mathrm{Inv}_{\mathrm{aux}}$, the feedforward voltage is obtained from the differential voltage between the grid and the main inverter $\mathrm{Inv}_{\mathrm{main}}$. The analysis above leads to the conclusion that the main inverter essentially functions as an ac voltage source with higher-order harmonics, and the responsibility for grid connection control actually falls on the auxiliary inverter. Consequently, it is feasible to analyze the parameters of the two inverters separately, resulting in the specifications given in Table I.

IV. Simulation and Experimental Results

A. Simulation Analysis and Results

In the advanced power system simulation software PSIM, comprehensive studies and modeling were conducted for both the traditional *L*-type grid-connected structure and the proposed two-segment inverter grid-connected structure. The specific parameters of the systems are detailed as shown in Table I.

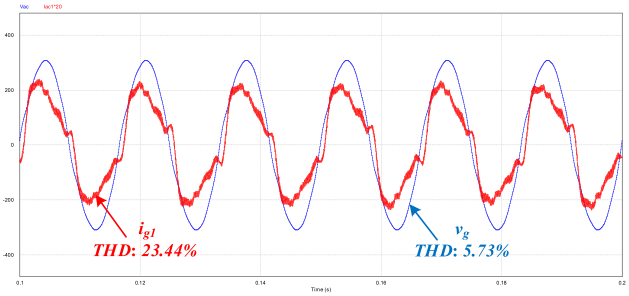

Fig. 14. Grid voltage and grid-connected current of L-type grid-connected inverter.

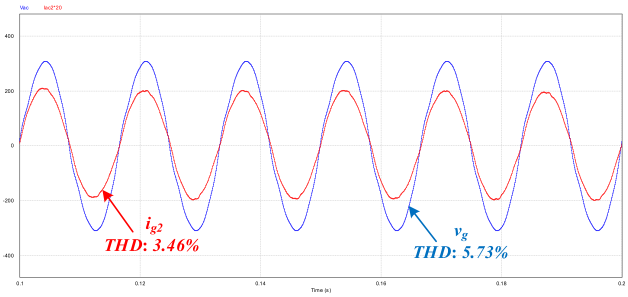

Fig. 15. Grid voltage and grid-connected current of the proposed two-segment grid-connected inverter.

To simulate the real grid environment more accurately, the fundamental frequency of the grid voltage was set at 220 V, and its harmonic content was meticulously modeled. The harmonic components incorporated were as follows: a third harmonic, labeled V_{g3}, possessing an amplitude of 10 V and an initial phase set at $\pi/3$; a fifth harmonic, referred to as V_{g5}, with an amplitude of 7 V and an initial phase of $\pi/4$; a seventh harmonic, designated as V_{g7}, also having an amplitude of 4 V and an initial phase of $\pi/4$. This setting not only reflects the complex scenarios the grid might encounter in reality but also aids in understanding the performance of grid-connected strategies when confronted with such harmonic disturbances. A series of simulation experiments were conducted, yielding the results shown in Figs. 14–16.

The simulation outcomes, as shown in Figs. 14–16, illustrate the comparative performance of a traditional L-type grid-connected inverter system and the proposed two-segment grid-connected inverter system. Fig. 14 presents the grid voltage v_g and grid current i_{g1} waveforms of the traditional L-type inverter system, where v_g has a THD of 5.73%, and notably, i_{g1} exhibits significant harmonic content with a THD of 23.44%. Such a THD level is typically deemed excessive for most grid-connected applications, indicating a relatively poor power quality due to the high harmonic content in the current. In contrast, Fig. 15 shows that the grid current i_{g2} of the proposed two-segment inverter lacks significant harmonic components, with the current waveform's THD markedly reduced to 3.46%. The decrease in THD indicates that the two-segment inverter is considerably effective in reducing harmonic distortion in the grid current, resulting in a higher power quality more suitable for grid-connected applications. Fig. 16(a) and (b) shows the system's grid-connected current response when the harmonic

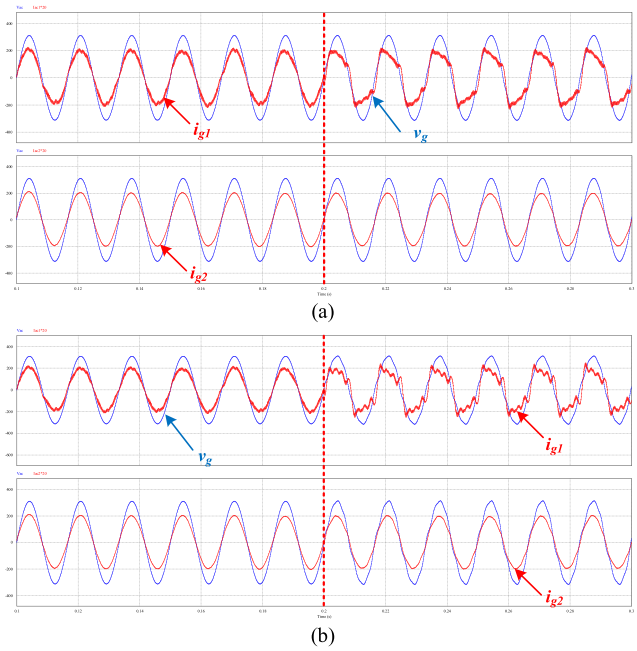

Fig. 16. Waveforms of the grid-connected voltage THD during sudden changes (a) 5.83% at 0.3 s. (b) 7.87% at 0.3 s.

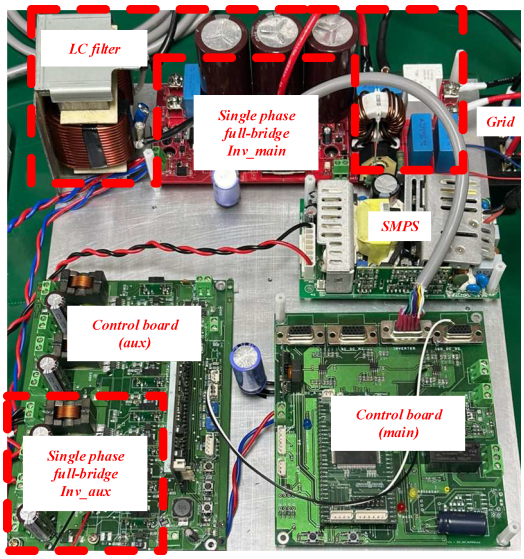

Fig. 17. Experimental prototype of two-segment grid-connected inverter.

content of the grid voltage suddenly increases to 5.83% and 7.87%, respectively. It can be seen that i_{g1} exhibits significant distortion as the harmonic content increases, with a noticeable rise in harmonic components in the waveform and a clear decline in power quality. In contrast, the current waveform of i_{g2} maintains good stability.

B. Experimental Analysis and Results

To verify the feasibility of the proposed grid-connected structure, a 3.3 KW experimental prototype was designed and manufactured, as shown in Fig. 17. The DSPTMS320F28335 was used

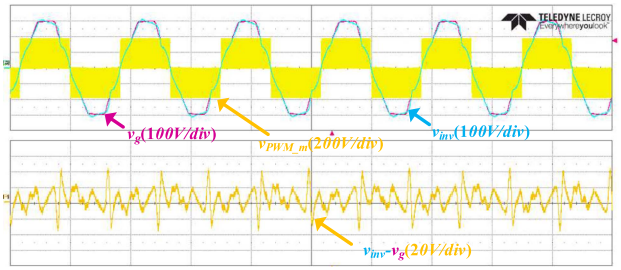

Fig. 18. Difference between output voltage of *L*-type grid-connected inverter and grid voltage.

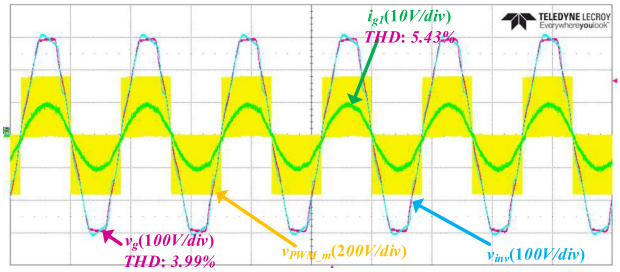

Fig. 19. Grid-connected current of *L*-type grid-connected inverter.

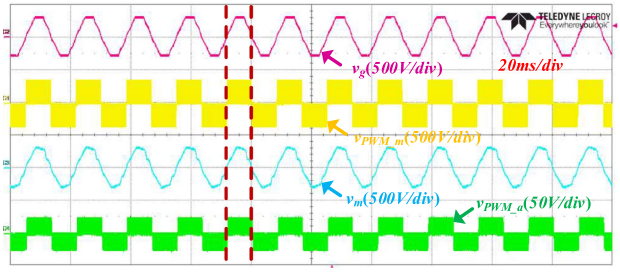

Fig. 20. Comparison of main inverter and auxiliary inverter.

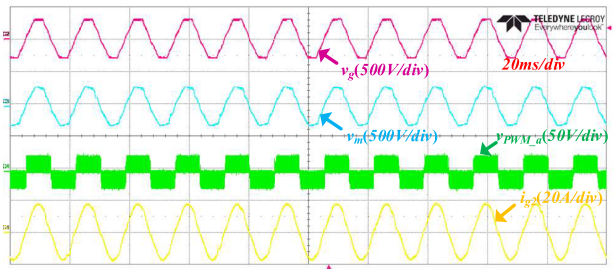

Fig. 21. Grid-connected current of the proposed two-segment grid-connected inverter.

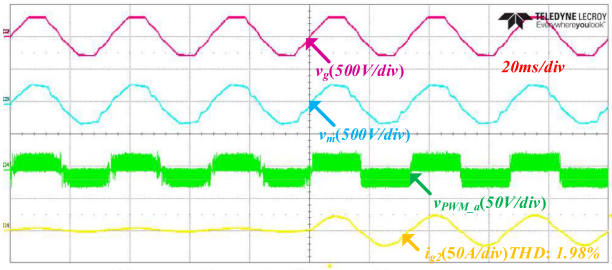

Fig. 22. Grid-connected action instant of the proposed two-segment grid-connected inverter when the grid-connecting current is 15 A.

as the main controller of the system, and the main parameters are also given in Table I.

As shown in Fig. 18, the actual grid voltage v_g is not a smooth sinusoidal waveform, but it is typical of an ac power source voltage. The actual output waveform of the inverter after filtering could not be obtained through measurement, as the voltage across the capacitor c_f is always clamped by the grid voltage. Therefore, the inverter's output voltage v_{inv} is obtained after digital-to-analog conversion. This is done to roughly discern the difference between the grid voltage and the inverter's output voltage. This differential waveform is a key parameter, as it represents the instantaneous difference between the grid and the inverter output, which needs to be minimized for effective synchronization with the grid. The v_{PWM} shows the active period of PWM, indicating that the inverter switches are "ON" and supplying power to the grid. Fig. 19 shows the steady-state waveform of the system under grid-connected mode at $P_{\text{ac}} = 3.3$ kW, with a THD of 3.99% for the grid voltage v_g. The figure shows that, influenced by the differential voltage, the grid current i_{g1} has a significant harmonic component with a THD of 5.43%. From Figs. 18 and 19, it is evident that the maximum difference between the grid voltage v_g and the inverter output voltage v_{inv} is 20 V, and the quality of the grid current i_{g1} is not high enough. Therefore, it is necessary to compensate for the difference between the grid voltage v_g and the inverter output voltage v_{inv} to reduce the voltage on the inductor L_f and thus improve the quality of the grid current.

In Fig. 20, the main inverter Inv_{main} outputs a waveform identical to the grid voltage, while the auxiliary inverter Inv_{aux} can generate a voltage in phase with the grid voltage. The experimental waveforms demonstrate that the voltage magnitude and phase of the Inv_{aux} are well controlled. This indicates that the differential voltage can be compensated through the voltage magnitude and phase of the Inv_{aux}. Fig. 21 shows the grid-connected condition of the proposed two-stage inverter when transferring 3.3 kW of power to the grid during a no-load connection process. It is observed that the grid current i_{g2} shows an improvement compared to i_{g1}. The output voltage of the Inv_{aux}, regulated by current control, can correct the differential voltage in real-time, ensuring the quality of the current fed into the grid.

The waveforms of the auxiliary transformer during grid-control startup at different grid-control currents are shown in Figs. 22 and 23. Initially, i_{g2} is flat at zero, indicating no current flow into the grid. The current starts to increase from zero, forming a sinusoidal shape. This ramp-up phase is critical and must be carefully controlled to prevent sudden surges or spike currents that could damage the grid or the inverter. The grid-connection process, as evidenced by i_{g2}, is exceptionally smooth, with no current fluctuations. This dynamic performance reflects the ability of the inverter for smooth startup and synchronization with the grid, demonstrating the effectiveness of

TABLE II
PERFORMANCE COMPARISON OF THE PROPOSED STRATEGY WITH OTHER STRATEGIES

	Power	Percentage of THD	Complexity	Implementation method	Control method	Efficiency
Proposed	3.3 kW	1.98%	Moderate	Hardware	Simple	95.8%
Guan et al. [8]	3 kW	3.13%	Moderate	Software	Moderate	Unknown
Bahra mi-Fard et al.[9]	0.6 kW	3.58%	Complex	Software+Hardware	Moderate	98.12%
Kan et al. [17]	3 kW	2.99%	Moderate	Software	Complex	High
Pourfa rrokh et al. [38]	1 kW	2.48%	Moderate	Hardware	Complex	93.93%
Srivastava and Seshad rinath [39]	1 kW	3.04%	Complex	Software+Hardware	Complex	96.25%
Rahimi et al. [40]	1 kW	3.2%	Complex	Software+Hardware	Moderate	96.16%

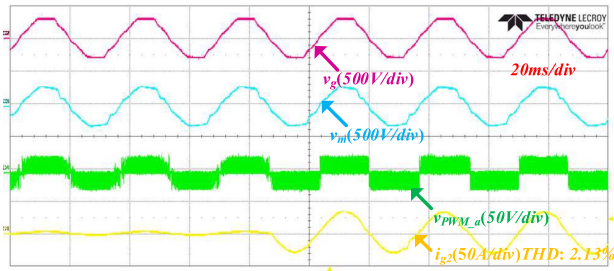

Fig. 23. Grid-connected action instant of the proposed two-segment grid-connected inverter when the grid-connecting current is 20 A.

TABLE III
PARAMETER COMPARISON

Power	LCL inverter	L inverter	Two-segment inverter
inductor	1.5 mH+1.5 mH	1.5 mH	1.5 mH+66 uH
capacitor	6.6 μF	6.6 μF	6.6 μF+10 μF
PWM method	unipolar SPWM	unipolar SPWM	unipolar SPWM+ bipolar SPWM
Switching frequency	10 kHz	16.6 kHz	16.6 kHz+20 kHz
Switch Type	IRGP6690DPbF	IRGP6690DPbF	IRGP6690DPbF+ IPP320N20N3

TABLE IV
LOSS COMPARISON

Loss	Two-segment inverter	LCL inverter	L inverter
On-off loss(W)	81.43	74.71	74.71
Switching loss(W)	11.15	6.98	25.8
Inductance loss(W)	42.72	82.33	42.36
Total loss(W)	135.26	163.95	142.88

the response and control strategy of the proposed two-segment grid-connected inverter. Table II compares the strategy proposed in this article with previous studies. It can be seen that the strategy proposed in this article provides high power output and performs exceptionally well in terms of THD, achieving 1.98%, which is significantly lower than other strategies. Although its efficiency is 95.8%, not the highest, considering its advantages in harmonic suppression, system implementation, and simplicity of control methods, the proposed strategy demonstrates significant overall performance advantages.

To verify the dynamic response characteristics of the proposed system, we connected the MX45-3PI-400-SNK device to the grid, capable of grid connection with any grid voltage containing arbitrary harmonic content. The experimental scenarios were set in three cases: First, the sudden change in grid-connected power was tested, where Fig. 24(a) and (b) shows the system's grid-connected response when the grid current rapidly increases from 10 to 20 A and decreases from 20 to 10 A, respectively. Second, the sudden change in grid voltage amplitude was tested, where Fig. 25(a) and (b) shows the system's grid-connected current response when the grid voltage amplitude changes suddenly. Finally, the sudden change in grid voltage THD was tested, where Fig. 26(a) and (b) shows the system's grid-connected current response when the grid voltage THD suddenly changes to 5.83% and 7.87%, respectively.

The experiments demonstrate that the system can respond quickly to sudden changes in grid-connected power, maintaining good current stability. When there is a sudden change in grid voltage amplitude, the system shows strong adaptability, with the current waveform remaining smooth. Furthermore, when there is a sudden change in grid harmonic frequency, the system can still effectively suppress harmonic distortion, ensuring current quality. This indicates the superior performance of the proposed two-stage grid connection method under various dynamic conditions.

C. Efficiency and Cost Analysis

To evaluate the efficiency of the proposed two-segment inverter, *LCL*-type PV grid-connected inverter and *L*-type PV grid-connected inverter models are constructed for efficiency comparison. In a 3 kW system at rated power, the parameters and losses of the proposed two-segment inverter, the *LCL*-type inverter, and the *L*-type inverter are shown in Tables III and IV, respectively.

From Table III, several observations can be made. First, the two-segment high-performance grid-connected inverter employs a more complex configuration of inductors and capacitors due to its dual inverter structure. Secondly, in terms of PWM methods, both the *LCL* inverter and *L*-type inverter use unipolar SPWM, whereas the two-segment high-performance inverter

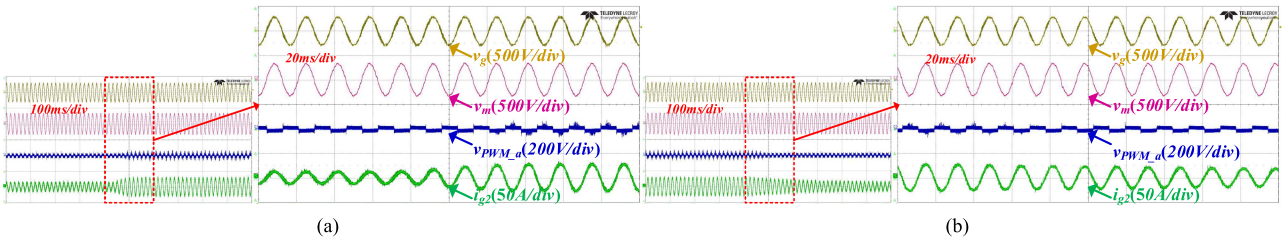

Fig. 24. Waveforms of the grid-connected current during sudden changes. (a) From 10 to 20 A. (b) From 20 A to 10 A.

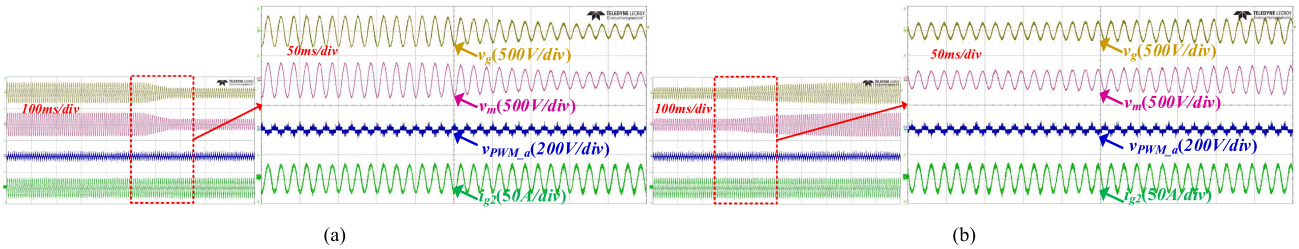

Fig. 25. Waveforms of the grid-connected voltage amplitude during sudden changes. (a) From 220 to 110 V. (b) From 110 to 220 V.

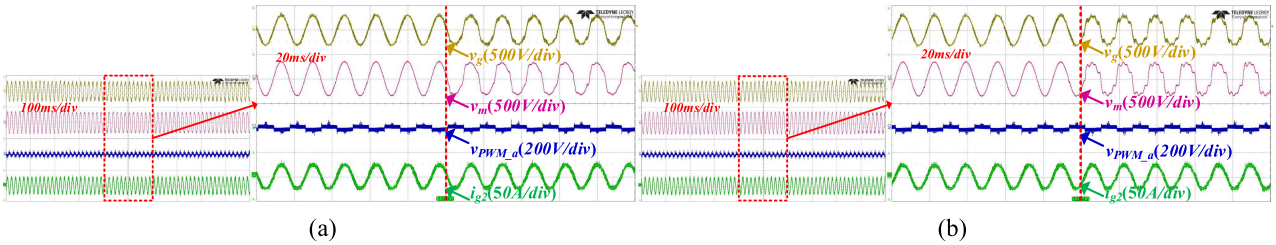

Fig. 26. Waveforms of the grid-connected voltage THD during sudden changes. (a) 5.83% at 0.3 s. (b) 7.87% at 0.3 s.

utilizes not only Unipolar SPWM, but also bipolar SPWM. This combination enables the two-segment high-performance inverter to achieve efficient voltage regulation and harmonic suppression under various operating conditions. Finally, the main and auxiliary inverters of the two-segment inverter operate at switching frequencies of 16.6 and 20 kHz, respectively. The higher switching frequencies significantly improve harmonic suppression and reduce losses caused by high-frequency harmonics.

From Table IV, it can be seen that the *LCL*-type grid-connected inverter is comparable to the two-segment grid-connected inverter in terms of conduction and switching losses. However, in terms of inductor losses, the *LCL*-type inverter has twice the losses of the two-segment inverter. For the *L*-type inverter, the set switching frequency of 10 kHz leads to a higher switching loss of about 14.65 W compared to the two-section inverter, under the condition that the THD of the grid current is kept below 5%. Since the number of switches in the two-section inverter is twice as many as the other two inverters, the conduction loss is higher. Nonetheless, the difference is not significant, so the total losses of the two-stage PV inverter are still the lowest under the 3 kW output power condition.

The efficiencies of the two-segment PV grid-connected inverter, *LCL*-type PV grid-connected inverter, and *L*-type PV grid-connected inverter are shown in Fig. 27 when the grid-connected current amplitude is changed from 10 to 20 A.

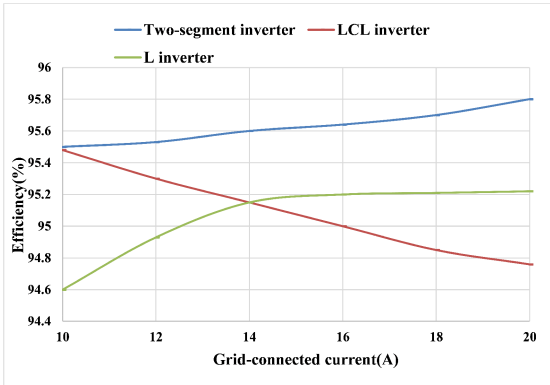

Fig. 27. Comparison of efficiency at different grid-connected current amplitudes.

From Fig. 27, it can be seen that the efficiency of the *L*-type inverter increases in the range of grid-connected currents from 10 to 20 A. Nevertheless, the efficiency of the *L*-type inverter is still lower than that of the two-segment PV inverter due to its relatively high switching losses. The *LCL*-type inverter has the

highest efficiency at a grid-connecting current of 10 A, but as the grid-connecting current increases, its inductive losses increase, resulting in a continuous decrease in efficiency. Among the three types of inverters, the two-segment PV grid-connected inverter has the highest efficiency and shows an increasing trend as the grid-connected current increases. Therefore, the use of two-segment grid-connected inverters in PV grid-connected systems can significantly improve the system efficiency.

V. Conclusion

The article designs a single-phase grid-connected system, consisting of a main inverter and an auxiliary inverter. The main inverter is directly controlled by the simplest closed-loop control based on the amplitude and phase of the grid voltage obtained. Meanwhile, the auxiliary inverter can quickly compensate for the differential voltage between the grid and the main inverter through PI control, ensuring the quality of the current injected into the grid, reducing voltage fluctuations on the grid inductor, and thereby improving the quality of the grid current. Compared to complex filtering structures, this scheme optimizes the overall system topology, primarily regarding efficiency, grid-connected current THD content, and control system complexity. Finally, a 3.3 kW experimental prototype was fabricated and tested to verify the effectiveness and stability of the proposed solution. This prototype provides excellent response characteristics and performance in grid-connected mode.

References

[1] G. I. Orfanoudakis, E. Lioudakis, G. Foteinopoulos, E. Koutroulis, and W. Wu, "Dynamic global maximum power point tracking for partially shaded PV arrays in grid-connected PV systems," *IEEE J. Emerg. Sel. Topics Ind. Electron.*, to be published, doi: 10.1109/JESTIE.2024.3389686.

[2] V. L. Srinivas, B. Singh, and S. Mishra, "Enhanced power quality PV inverter with leakage current suppression for three-phase SECS," *IEEE Trans. Ind. Electron.*, vol. 69, no. 6, pp. 5756–5767, Jun. 2022.

[3] P. Ray, P. K. Ray, and S. K. Dash, "Power quality enhancement and power flow analysis of a PV integrated UPQC system in a distribution network," *IEEE Trans. Ind. Appl.*, vol. 58, no. 1, pp. 201–211, Jan./Feb. 2022.

[4] C. Li, J. Zhang, and H. Wen, "Accurate and fast amplitude estimation of signal distorted by noise and harmonics for control of VSI," *IEEE Trans. Ind. Electron.*, vol. 68, no. 12, pp. 12584–12594, Dec. 2021.

[5] S. Kan, X. Ruan, X. Huang, and H. Dang, "Second harmonic current reduction for flying capacitor clamped boost three-level converter in photovoltaic grid-connected inverter," *IEEE Trans. Power Electron.*, vol. 36, no. 2, pp. 1669–1679, Feb. 2021.

[6] S. Albatran, A. R. Al Khalaileh, and A. S. Allabadi, "Minimizing total harmonic distortion of a two-level voltage source inverter using optimal third harmonic injection," *IEEE Trans. Power Electron.*, vol. 35, no. 3, pp. 3287–3297, Mar. 2020.

[7] L. B. G. Campanhol, S. A. O. Da Silva, A. A. De Oliveira, and V. D. Bacon, "Power flow and stability analyses of a multifunctional distributed generation system integrating a photovoltaic system with unified power quality conditioner," *IEEE Trans. Power Electron.*, vol. 34, no. 7, pp. 6241–6256, Jul. 2019.

[8] Y. Guan, Y. Wang, Y. Xie, Y. Liang, A. Lin, and X. Wang, "The dual-current control strategy of grid-connected inverter with LCL filter," *IEEE Trans. Power Electron.*, vol. 34, no. 6, pp. 5940–5952, Jun. 2019.

[9] M. Bahrami-Fard, N. Moeini, M. Shahabadini, and H. Iman-Eini, "A filter-based topology and modulation strategy with leakage current mitigation for grid-connected CHB photovoltaic inverters," *IEEE Trans. Power Electron.*, vol. 39, no. 9, pp. 11164–11175, Sep. 2024.

[10] X. Huang, X. Ruan, L. Zhang, and F. Liu, "Second harmonic current reduction schemes for DC-DC converter in two-stage PFC converters," *IEEE Trans. Power Electron.*, vol. 37, no. 1, pp. 332–343, Jan. 2022.

[11] L. Zhang and X. Ruan, "Control schemes for reducing second harmonic current in two-stage single-phase converter: An overview from DC-bus port-impedance characteristics," *IEEE Trans. Power Electron.*, vol. 34, no. 10, pp. 10341–10358, Oct. 2019.

[12] F. Liu, X. Ruan, X. Huang, Y. Qiu, and Y. Jiang, "Control scheme for reducing second harmonic current in AC-DC-AC converter system," *IEEE Trans. Power Electron.*, vol. 37, no. 3, pp. 2593–2605, Mar. 2022.

[13] X. Meng, Y. Jia, C. Ren, X. Han, and P. Wang, "Modular circulating current and second harmonic current suppression strategy by virtual impedance for DC solid-state transformer," *IEEE Trans. Power Electron.*, vol. 36, no. 10, pp. 11921–11933, Oct. 2021.

[14] H. Zhou, L. He, and F. Lu, "Impedance editing based second harmonic current reduction for new energy access system," *IEEE Trans. Ind. Electron.*, vol. 71, no. 3, pp. 2638–2649, Mar. 2024.

[15] L. Zhang, X. Ruan, and X. Ren, "One-cycle control for electrolytic capacitor-less second harmonic current compensator," *IEEE Trans. Power Electron.*, vol. 33, no. 2, pp. 1724–1739, Feb. 2018.

[16] F. Liu, X. Ruan, X. Huang, and Y. Qiu, "Second harmonic current reduction for two-stage inverter with DCX-LLC resonant converter in front-end DC-DC converter: Modeling and control," *IEEE Trans. Power Electron.*, vol. 36, no. 4, pp. 4597–4609, Apr. 2021.

[17] S. Kan, X. Ruan, H. Dang, L. Zhang, and X. Huang, "Second harmonic current reduction in front-end DC-DC converter for two-stage single-phase photovoltaic grid-connected inverter," *IEEE Trans. Power Electron.*, vol. 34, no. 7, pp. 6399–6410, Jul. 2019.

[18] K. Jia, J. Chen, G. Zhao, B. Yang, and T. Bi, "Second harmonic injection-based recovery control of PV DC boosting integration system," *IEEE Trans. Smart Grid*, vol. 12, no. 2, pp. 1022–1032, Mar. 2021.

[19] A. Kulkarni and S. K. Mazumder, "Deadtime elimination in a GaN-based grid-connected differential-mode ĆUK inverter," *IEEE Trans. Ind. Electron.*, vol. 66, no. 4, pp. 3296–3302, Apr. 2019.

[20] D. Townsend, G. Mirzaeva, and G. C. Goodwin, "Deadtime Compensation for model predictive control of power inverters," *IEEE Trans. Power Electron.*, vol. 32, no. 9, pp. 7325–7337, Sep. 2017.

[21] J. H. Lee and S. K. Sul, "Inverter nonlinearity compensation through deadtime effect estimation," *IEEE Trans. Power Electron.*, vol. 36, no. 9, pp. 10684–10694, Sep. 2021.

[22] Z. Tang et al., "Modulation for the AVC-HERIC inverter to compensate for deadtime and minimum pulsewidth limitation distortions," *IEEE Trans. Power Electron.*, vol. 35, no. 3, pp. 2571–2584, Mar. 2020.

[23] D. Xiang, J. Yang, Y. Hao, and G. Xu, "Two-parameter identification method of deadtime effect voltage error model during self-commission," *IEEE Trans. Power Electron.*, vol. 38, no. 12, pp. 15904–15920, Dec. 2023.

[24] Z. Zheng, L. Zhang, C. Wu, Y. Wang, Z. Lei, and K. Sun, "Variable OFF-time and deadtime scheme with optimized control frequency for soft-switching single-phase inverters," *IEEE Trans. Power Electron.*, vol. 38, no. 4, pp. 4972–4987, Apr. 2023.

[25] W. Ma, Y. Guan, B. Zhang, and L. Wu, "Active disturbance rejection control based single current feedback resonance damping strategy for LCL-type grid-connected inverter," *IEEE Trans. Energy Convers.*, vol. 36, no. 1, pp. 48–62, Mar. 2021.

[26] T. V. Tran, K. H. Kim, and J. S. Lai, "Optimized active disturbance rejection control with resonant extended state observer for grid voltage sensorless LCL-filtered inverter," *IEEE Trans. Power Electron.*, vol. 36, no. 11, pp. 13317–13331, Nov. 2021.

[27] M. S. Karbasforooshan and M. Monfared, "Adaptive self-tuned current controller design for an LCL-filtered LC-tuned single-phase shunt hybrid active power filter," *IEEE Trans. Power Del.*, vol. 37, no. 4, pp. 2747–2756, Aug. 2022.

[28] S. Bosch, J. Staiger, and H. Steinhart, "Predictive current control for an active power filter with LCL-filter," *IEEE Trans. Ind. Electron.*, vol. 65, no. 6, pp. 4943–4952, Jun. 2018.

[29] J. Fang, X. Li, X. Yang, and Y. Tang, "An integrated trap-LCL filter with reduced current harmonics for grid-connected converters under weak grid conditions," *IEEE Trans. Power Electron.*, vol. 32, no. 11, pp. 8446–8457, Nov. 2017.

[30] Z. Zhang et al., "Principle and robust impedance-based design of grid-tied inverter with LLCL-filter under wide variation of grid-reactance," *IEEE Trans. Power Electron.*, vol. 34, no. 5, pp. 4362–4374, May 2019.

[31] S. Jiang, Y. Liu, W. Liang, J. Peng, and H. Jiang, "Active EMI filter design with a modified LCL-LC filter for single-phase grid-connected inverter in vehicle-to-grid application," *IEEE Trans. Veh. Technol.*, vol. 68, no. 11, pp. 10639–10650, Nov. 2019.

[32] Y. Ye and Y. Xiong, "UDE-based current control strategy for LCCL-type grid-tied inverters," *IEEE Trans. Ind. Electron.*, vol. 65, no. 5, pp. 4061–4069, May 2018.

[33] J. Xu, J. Yang, J. Ye, Z. Zhang, and A. Shen, "An LTCL filter for three-phase grid-connected converters," *IEEE Trans. Power Electron.*, vol. 29, no. 8, pp. 4322–4338, 2014.

[34] H. Zhang, X. Ruan, Z. Lin, L. Wu, Y. Ding, and Y. Guo, "Capacitor voltage full feedback scheme for LCL-type grid-connected inverter to suppress current distortion due to grid voltage harmonics," *IEEE Trans. Power Electron.*, vol. 36, no. 3, pp. 2996–3006, Mar. 2021.

[35] M. Liserre, R. Teodorescu, and F. Blaabjerg, "Multiple harmonics control for three-phase grid converter systems with the use of PI-RES current controller in a rotating frame," *IEEE Trans. Power Electron.*, vol. 21, no. 3, pp. 836–841, May 2006.

[36] Z. Lin, X. Ruan, L. Wu, H. Zhang, and W. Li, "Multi resonant component-based grid-voltage-weighted feedforward scheme for grid-connected inverter to suppress the injected grid current harmonics under weak grid," *IEEE Trans. Power Electron.*, vol. 35, no. 9, pp. 9786–9795, Sep. 2020.

[37] W. Li, X. Ruan, D. Pan, and X. Wang, "Full-feedforward schemes of grid voltages for a three-phase LCL-type grid-connected inverter," *IEEE Trans. Ind. Electron.*, vol. 60, no. 6, pp. 2237–2250, 2013.

[38] S. Pourfarrokh, J. Adabi, and F. Zare, "A new grid-connected asymmetrical multilevel converter for PV application," *IEEE Trans. Power Electron.*, vol. 39, no. 9, pp. 11256–11265, Sep. 2024.

[39] A. Srivastava and J. Seshadrinath, "A single-phase seven-level triple boost inverter for grid-connected transformerless PV applications," *IEEE Trans. Ind. Electron.*, vol. 70, no. 9, pp. 9004–9015, Sep. 2023.

[40] R. Rahimi, M. Farhadi, G. R. Moradi, B. Farhangi, and S. Farhangi, "Three-phase filter-clamped transformerless inverter for grid-connected photovoltaic systems with low leakage current," *IEEE Trans. Ind. Appl.*, to be published, doi: 10.1109/TIA.2020.3008134.